International Journal of Nanomedicine Dovepress

Open Access Full Text Article ORIGINAL RESEARCH

A Multifunctional Low-Temperature Photothermal Nanomedicine for Melanoma Treatment via the Oxidative Stress Pathway Therapy

Dou Zhang[1,2,*], Xuyi Liu[1,2,*], Xiong Li[3,*], Xinyi Cai[1,2], Zhenying Diao[1,2], Long Qiu[1,2], Xuelin Chen[1,2], Yuyu Liu[1,2], Jianbo Sun[1], Daxiang Cui[1,4], Qiaoyuan Ye[5], Ting Yin[1,2]

[1]Research Center of Nano Technology and Application Engineering, The First Dongguan Affiliated Hospital, School of Pharmacy, Guangdong Medical University, Dongguan, Guangdong, 523808, People's Republic of China; [2]Dongguan Biomedical Nano Engineering Technology Research Center, Guangdong Medical University, Dongguan, Guangdong, 523808, People's Republic of China; [3]Department of Pharmacy, Zhuhai People's Hospital (Zhuhai Hospital Affiliated with Jinan University), Zhuhai, Guangdong, 519000, People's Republic of China; [4]School of Sensing Science and Engineering, School of Electronic Information and Electrical Engineering, Shanghai Jiao Tong University, Shanghai, 200240, People's Republic of China; [5]Department of Dermatology and Venereology, Second Clinical Medical College of Guangdong Medical University, Dongguan, Guangdong, 523808, People's Republic of China

*These authors contributed equally to this work

Correspondence: Qiaoyuan Ye, Department of Dermatology and Venereology, Second Clinical Medical College of Guangdong Medical University, Dongguan, Guangdong, 523808, People's Republic of China, Email 13650248189@163.com; Ting Yin, Research Center of Nano Technology and Application Engineering, School of Pharmacy, Guangdong Medical University, Dongguan, Guangdong, 523808, People's Republic of China, Email wsyt132@163.com

Purpose: Melanoma is a highly aggressive and dangerous malignant skin tumor and there is an urgent need to develop effective therapeutic approaches against melanoma. The main objective of this study was to construct a multifunctional nanomedicine (GNR@PEG-Qu) to investigate its therapeutic effect on melanoma from the oxidative stress pathway.

Methods: First, the nanomedicine GNR@PEG-Qu was synthesized and characterized, and its photothermal and antioxidant properties were confirmed. In addition, in vivo imaging capabilities were observed. Finally, the tumor inhibitory effects of GNR@PEG-Qu in vivo and in vitro as well as its biosafety were observed.

Results: GNR@PEG-Qu shows good photothermal and anti-oxidation properties. Following exposure to 1064 nm laser irradiation in the second near-infrared II (NIR-II) window, GNR@PEG-Qu shows anti-tumor ability through low-temperature photothermal therapy (PTT) adjuvant drug chemotherapy. GNR@PEG-Qu makes full use of the antioxidant capacity of quercetin, reduces ROS levels in melanoma, alleviates oxidative stress state, and achieves "oxidative stress avoidance" at the tumor site. Quercetin can also down-regulate the expression of the heat shock protein Hsp70, which will improve the thermal sensitivity of the tumor site and enhance the efficacy of low-temperature PTT.

Conclusion: GNR@PEG-Qu nanoagent exhibits synergistic treatment and high tumor inhibition effects, which is a promising strategy developed to achieve oxidative stress avoidance and synergistic therapy of melanoma using quercetin (Qu)-coated gold nanorod (GNR@PEG).

Keywords: melanoma, gold nanorods, quercetin, chemo-photothermal therapy, oxidative stress

Introduction

Melanoma is a common malignant skin tumor that is highly aggressive and dangerous.[1,2] In clinical practice, the traditional treatment of melanoma is limited to surgical excision,[3] chemotherapy,[4,5] and radiotherapy,[6,7] but the prognosis remains poor because of incomplete clearance, side effects, and easy recurrence.[8,9] Therefore, effective treatments are urgently required to combat melanoma. Previous studies have shown that the main cause of melanoma development is related to increased reactive oxygen species (ROS) levels, oxidative stress, and redox imbalance.[10,11] Epidermal melanocytes are susceptible to oxidative stress because of the high generation of ROS during melanin biosynthesis

Received: 21 July 2024
Accepted: 30 October 2024
Published: 11 November 2024

and UV radiation. Melanocytes are unable to adequately counteract the dramatic increase in ROS levels and oxidative stress, leading to DNA and lipid damage, which induces DNA repair or tumor-initiating cell production.[12] Hence, increased levels of ROS contribute to the entire process of melanoma formation and play a role in drug resistance.[13] Accordingly, inhibiting melanoma development by modulating ROS levels and oxidative stress pathways is considered to represent a promising therapeutic approach.

Photothermal therapy (PTT) has drawn attention owing to the utilization of near-infrared (NIR) light-absorbing materials, which enables precise control of the time and area during the treatment of diseases and thermogenic cytotoxicity.[14–16] PTT is an effective cancer treatment that utilizes infrared wavelength-induced thermotherapy to kill cancer cells.[17,18] PTT is characterized by noninvasiveness, low toxicity, and high efficiency compared to traditional cancer treatments such as radiotherapy and chemotherapy.[19,20] The complete ablation of tumors generally requires high temperatures of 50 °C or more.[21] Photothermal temperatures induced by large doses of nanoparticles or laser irradiation may lead to cellular necrosis and induce inflammatory disorders on account of nonspecific heating and unavoidable thermal diffusion,[22,23] threatening normal cells and tissues in the vicinity,[24] and even inducing tumor metastasis and growth.[25] Although lower temperatures (42–45 °C) can also cause thermal damage to cells, this type of damage, which results from insufficient heat, can be repaired by heat shock protein (Hsp)-mediated thermal resistance.[26,27] Low temperature induces the expression of most HSPs, making cancer cells insensitive to heat and affecting the therapeutic effect of PTT.[28] In addition, low temperature is not effective in killing cancer cells and even exhibits heat resistance. Therefore, the development of effective PTT strategies is important in the clinical application of tumor ablation.[29,30] Currently, low-temperature PTT uses photothermal materials loaded with inhibitors to curb Hsp expression and overcome tumor thermal resistance. This achieves effective tumor killing at low temperature, demonstrating an effective thermotherapy strategy.[28,31,32] For example, Ma et al. Proposed using an aggregation-induced emission (AIE) nanobomb to inhibit the upregulated expression of HSPs during low-temperature PTT by releasing carbon monoxide (CO) in the tumor microenvironment to improve the anti-tumor efficiency.[33] Moreover, Sun et al demonstrated that phototherapeutic nanoparticles loaded with the Hsp inhibitor tanespimycin (17-AAG) could unload the inhibitor at the tumor site after intravenous injection to enhance the thermal sensitivity of tumor cells. The precise regulation of the internal temperature in the tumor during the PTT process can ultimately lead to efficient and safe tumor PTT.[34] However, these strategies can be achieved by loading Hsp inhibitors or by directly eliminating HSPs, but their loading capacity,[35] release efficiency, and Hsp consumption are problematic. The potential for clinical applications is far from satisfactory.

Inspired by these issues and to validate the above-mentioned conjectures, it will be important to prepare efficient nanoparticles consisting of PTT reagents, Hsp inhibitors, and antioxidant reagents. However, this complex system raises further concerns about potential toxicity and biocompatibility, hindering its future clinical applications. Therefore, we plan to design a simple and versatile nanoparticle to realize these ideas. First, gold nanorods (GNR) were selected as the photothermal agent to exert the PTT effect. GNR is a classical photothermal material with high photothermal conversion efficiency, excellent photothermal stability, and great potential in PTT of cancer.[36,37] Subsequently, quercetin was selected as the main component of the nano-photothermite through the evaluation of effective bioactive phenolic compounds (Table S1).[38–47] Quercetin (3,5,7,30,40-pentahydroxyflavone) is an important class of flavonoids with abundant hydroxyl groups and excellent antioxidant capacity. It is therefore considered to be a promising anticancer drug.[46,48,49] The ability of quercetin to prevent the proliferation of various tumor cells has been documented owing to its excellent antioxidant activity and ability to regulate tumor suppressor genes.[50,51] Notably, the cytotoxicity of quercetin on normal cells is negligible, even at high levels. Based on these properties, quercetin is a promising drug for the treatment of various tumors. The use of quercetin in PTT has several advantages. First, quercetin is widely found in fruits and vegetables, which demonstrates its good biosafety.[52] Second, quercetin is known to be a potent inhibitor of HSPs,[53] which can interfere with the phosphorylation of heat shock transcription factors to inhibit the expression of Hsp70,[54] representing a significant advantage for low-temperature PTT.[53–56] In addition, the proliferation of different types of tumor cells, such as breast cancer, lung cancer, melanoma, and glioblastoma, can be inhibited by the anticancer and antioxidant properties of quercetin.[36,57] Quercetin is an excellent antioxidant that can scavenge overexpressed ROS and reduce oxidative stress in tumors,[51,58,59] thereby avoiding oxidative stress and aiming to treat tumors through the oxidative stress pathway. This is important for treating melanoma. Although previous studies have demonstrated that

the proliferation of B16F10 melanoma cells can be inhibited by quercetin, our understanding of the multiple functions of quercetin in B16F10 melanoma cells is incomplete.

Here, we propose a photothermal nanoagent (GNR@PEG-Qu) for melanoma therapy. This nanoagent can overcome the shortcomings of low-temperature PTT, improve the tumor microenvironment of melanoma, and achieve a synergistic combination of chemotherapy and PTT, which ultimately enhances the anti-tumor effect. Meanwhile, GNR@PEG-Qu fully exerts its antioxidant effect to improve the oxidative stress state in melanoma treatment and precisely responds to the high expression of ROS to block the development of melanoma. The synthesis process of GNR@PEG-Qu is shown in Scheme 1. Briefly, GNR was synthesized by the seed generation method using acid tetrachloroaurate ($HAuCl_4$), cetyltrimethylammonium bromide (CTAB), and ascorbic acid as raw materials and active agents. Because of the high toxicity of CTAB, SH-PEG_{5K}-COOH was used to replace CTAB. Subsequently, quercetin was introduced for loading through electrostatic interactions. In this study, the anticancer activity of GNR@PEG-Qu was demonstrated by in vitro experiments using B16F10 cells. In addition, after injection via the tail vein in in vivo experiments, the prepared nanoparticles accumulated at the tumor site and were effectively absorbed by the cancer cells. After irradiation of the tumor site with a NIR laser, GNR@PEG-Qu mediated low-temperature PTT combined with chemotherapy strengthens the therapeutic effect, and oxidative stress avoidance is precisely applied to melanoma, which is ultimately treated effectively. The research verified that GNR@PEG-Qu has significant advantages in vitro and in vivo: (1) efficient low temperature PTT; (2) synergistic anticancer efficacy; and (3) oxidative stress resistance. The integration of these advantages makes GNR@PEG-Qu nanodrugs available for effective cancer therapy.

Materials and Methods

Reagents

Acid tetrachloroaurate ($HAuCl_4$), sodium borohydride ($NaBH_4$), and cetyltrimethylammonium bromide (CTAB) were purchased from national medicines Co. Ltd (China). Quercetin (Qu) was purchased from Aladdin Reagents Co., Ltd. Calcein-AM/PI dead-live staining kit, 1 × PBS (0.01 M, pH 7.2–7.4), trypsin without EDTA, penicillin-streptomycin, radioimmunoprecipitation assay (RIPA) buffer, polyvinylidene difluoride membranes (PVDF), and BCA Protein Assay Kit were obtained from Solarbio (Beijing, China). Annexin V-FITC/PI Cell Apoptosis Kit was obtained from KAIJI (China), and 4,6-Diamidino-2-phenylindole (DAPI) was purchased from Beyotime Biotechnology. TNF-α, IL-6, and Hsp70 ELISA kits were purchased from Jiangsu Meimian Industrial Co., Ltd.

Cell Lines and Animals

Murine melanoma cell line B16F10 were originally obtained from American Type Culture Collection (ATCC). B16F10 cells were incubated in complete medium prepared with 10% fetal bovine serum (FBS), 90% Dulbecco's modified Eagle medium (DMEM), and 1% penicillin/streptomycin (100 U/mL). A humidified incubator containing 5% CO_2 was used to culture the cells. Female C57BL/6 mice 6–8 weeks old, weighing 18–23 g were purchased from Zhuhai BesTest Bio-Tech Co, Ltd. Subsequently, they were housed in an SPF-grade barrier environment with a temperature of 20–28 °C, a relative humidity of 55%, and a 12-h light/dark cycle. All mouse studies were performed under the Guide for Care and Use of Laboratory Animals, and all animal experiments were performed in accordance with the current guidelines and ethical considerations that were approved by the Laboratory Animal Center of Guangdong Medical University (GDMU-2023-000077). All animals were treated humanely throughout the experimental period.

Synthesis of GNR@PEG-Qu

First, GNR were synthesized using the seed-mediated growth method.[36,60,61] Briefly, $HAuCl_4$ (0.25 mL, 0.01 mol/L) was added to CTAB (9.75 mL, 0.1 mol/L). Then, $NaBH_4$ (600 μL, 0.01 mol/L) in ice water was rapidly added to the above solution under vigorous stirring with a magnetic stirrer. The color of the solution changed from yellow to brown, indicating the formation of gold seeds. Stirring was continued for 2 min to obtain the gold seed solution, and the gold seeds were obtained after standing at room temperature for 3 h. Subsequently, $HAuCl_4$ solution (0.5 mL, 0.01 mol/L), silver nitrate ($AgNO_3$) (0.1 mL, 0.01 mol/L), and H_2SO_4 (0.2 mL, 0.5 mol/L) were added to CTAB (9 mL, 0.1 mol/L). After mixing well, ascorbic acid (AA) solution (0.08 mL, 0.1 mol/L) was added, and seed solution (1 mL) was quickly

added after stirring for 2 min with a magnetic stirrer. The above solution was left at room temperature overnight and then centrifuged at 10,000 rpm for 3 min. The supernatant was removed, and the gold nanorods were separated by centrifugation with pure water twice. SH-PEG_{5K}-COOH was added to the gold nanorod solution and stirred on a magnetic stirrer for 24 h to obtain GNR@PEG. Quercetin solution dissolved in DMSO was added and stirred for 6 h. The solution was transferred to an ultrafiltration tube (100 KD) for ultrafiltration (3500 rpm, 15 min), and the solution was collected after washing twice with pure water to obtain GNR@PEG-Qu.

Characterization and Photothermal Evaluation of GNR@PEG-Qu

The morphology of the nanoparticles and UV-vis spectra were measured by TEM (H-6009IV, Japan) and a HITACHI UH5700 spectrophotometer, respectively. A particle sizer (Nano-ZS90, UK) was used to analyze the hydrodynamic particle size and zeta potential of GNR@PEG-Qu. To investigate the photothermal effect of GNR@PEG-Qu, 300 mL of sample (GNR@PEG and GNR@PEG-Qu) containing a GNR@PEG solution (0.02 mg/mL) was dispersed in water and irradiated with a 1064-nm NIR laser (power of 1.0 W/cm^2) for 5 min. The solution temperature was recorded at each time point using a thermal imager (HIKMICRO, China). PBS was used as the control. The thermal camera also captured photothermal images. Similarly, the temperature rise changes in GNR@PEG-Qu were recorded at different concentrations or powers. The thermal stability of GNR@PEG-Qu was evaluated. GNR@PEG-Qu (0.3 mL 0.02 mg/mL) was irradiated by a laser at 1.0 W/cm^2 for 5 min, and the solution was allowed to cool naturally. The procedure was repeated five times, and the temperature variation of the solution was recorded in real time using the thermal imager. Finally, the photothermal conversion efficiency (η) of GNR@PEG-Qu was calculated.

In vitro Cellular Uptake Assay

Cellular uptake of GNR@PEG-Qu (marked by Cy5.5) in vitro was observed using CLSM and flow cytometry. For intracellular localization imaging, confocal dishes were used to incubate B16F10 cells. The cells were inoculated overnight and then administered GNR@PEG-Qu at different time intervals. Subsequently, the cells were washed twice with PBS and incubated with Hoechst 33342 for 10 min for nuclear localization. Finally, the cellular uptake was observed and photographed by CLSM. Similarly, B16F10 cells were cultured in 24-well plates (1×10^5 cells/well). After overnight incubation, the cells were incubated with fresh medium containing GNR@PEG-Qu. Subsequently, the cells were incubated with GNR@PEG-Qu for different time intervals. Furthermore, all cells were collected by centrifugation, washed once with PBS, and dispersed in PBS. Then, flow cytometry (BD FACSAria III) was used for sample uptake and quantitative analysis.

Cytotoxicity Assay

First, the CCK-8 method was used to assess the cytotoxicity and photothermal efficiency of GNR@PEG-Qu on B16F10 cell lines. The cells were collected after the underside of the culture flask was grown and covered by B16F10 cells. The cells were subsequently inoculated in 96-well plates at a density of 1×10^4 cells per well. After overnight incubation, the medium in the well plates was replaced with complete medium containing different concentrations of samples. After 4 h of drug administration, the laser groups were irradiated with 1064-nm laser (1.0 W/cm^2) for 5 min. The cells were incubated in an incubator for 20 h, and then the original medium was replaced with a medium containing CCK-8. After the scheduled time, the absorbance of the sample at 450 nm was measured using a microplate reader (ELISA of PerkinElmer). All groups were repeated five times to obtain the mean values. The cell viability and combination index (CI)[62–64] were defined using the following equations:

$$\text{Cell viability}(\%) = \frac{\text{ODsample}}{\text{ODcontrol}} \times 100\%$$

where OD_{sample} is the OD value in the presence of the sample, and $OD_{control}$ is the OD value of the control group.

$$\text{CI} = \frac{IC50(combinedtherapy)}{IC50(chemotherapyalone)} + \frac{IC50(combinedtherapy)}{IC50(PTTalone)}$$

where IC50 indicates the semi-inhibited concentration of the preparation. Furthermore, the cytotoxicity of GNR@PEG-Qu was detected using the live-dead staining kit. Cells from different administration groups were stained with Calcein-AM and PI according to the instructions. Images were taken using a live cell imager.

Apoptosis Detection

To determine the cytotoxicity of GNR@PEG-Qu, the Annexin V-FITC/PI Apoptosis Detection Kit was used to detect apoptotic cells. After 12 h of incubation, the B16F10 cells were treated with (1) PBS; (2) Qu (300 μg/mL); (3) GNR@PEG-Qu (10 μg/mL of GNR@PEG and 300 μg/mL Qu); (4) GNR@PEG+NIR (10 μg/mL of GNR@PEG); and (5) GNR@PEG-Qu+NIR (10 μg/mL of GNR@PEG and 300 μg/mL Qu) at 37 °C for 24 h. Cells categorized into the light group were irradiated with a 1064-nm laser (1.0W/cm^2) for 5 min and then cultured in an incubator. All cells were collected 12 h later, washed with PBS, and stained using the kit. The stained cells were incubated at room temperature under dark conditions for 15 min, and then the cells were washed immediately and detected by flow cytometry.

Western Blot Assay

Total proteins were harvested from B16F10 cells. Hsp70 expression levels were analyzed by Western blotting. After seeding into 6-well plates and culturing overnight, B16F10 cells were grown with different samples for 24 h. The cells were then digested, collected, washed twice, and lysed in RIPA buffer containing protease inhibitors. The protein content in the different samples was quantified using a BCA protein kit, and subsequently, the sample proteins were treated and incubated with Hsp70 and actin. Goat anti-rabbit antibody was used as the secondary antibody and incubated again. Images were captured using a CLINX 6100 and analyzed manually with Servicebio software (AIWBwell TM). ImageJ software was used to quantify protein band density, and actin was used as an upsampling control.

In vitro ROS Elimination and Anti-Inflammatory Effects

B16F10 cells were cultured in four-compartment confocal dishes (2×10^4 cells/compartment) and incubated overnight with culture medium containing 1 mmol/L H_2O_2. The cells were then treated with culture medium containing different samples for 24 h. Subsequently, the ROS content in the cells was detected using DCFH-DA reagent (10 μm), and the images were captured on CLSM.

Animal and Tumor Models

To establish the tumor-bearing xenograft mouse model, B16F10 cell suspensions were suspended at a density of 1.0×10^6 cells in PBS (100 μL), and the xenografts were established by subcutaneous injection on the right flank of 6–8-week-old female C57BL/6 mice. Vernier calipers were used for measuring the tumor volume. The following formula was used to calculate the tumor volume: $V = A \times B^2 / 2$ (A refers to the shortest diameter of tumors, and B refers to the longest diameter of tumors). When the mouse tumors grew to a volume over 80–100 mm^3, the mice were assigned to different groups randomly: (1) PBS, (2) Qu, (3) GNR@PEG-Qu, (4) GNR@PEG+NIR, and (5) GNR@PEG-Qu+NIR. Then, tumor-bearing mice (n = 5 mice per group) were administered with intravenous injection of different formulations (100 μL per mouse). After injection for 4 and 24 h, the mice in groups 4 and 5 requiring laser irradiation were exposed to the laser for 5 min (1.5 W/cm^2), and photographs were simultaneously captured by a thermal imager. Groups (1), (2), and (3), as controls, did not experience any NIR irradiation. Tumor volumes were measured every day, and the mouse weight was measured every other day for 16 days, while representative photos of tumor-bearing mice were captured. Finally, the mice were humanely killed, and the tumors were harvested. Subsequently, tumors and the heart, liver, spleen, lungs, and kidneys were removed and fixed in 4% paraformaldehyde solution for histopathological analysis. Blood was collected from the eyes of mice for hematological analysis, and the PBS group was used as a control. Blood was centrifuged to obtain serum, and the levels of liver and kidney indices were determined using an enzyme-linked immunosorbent assay (ELISA). Similarly, the HIF-α, TNF-α, and IL-6 in serum were measured using ELISA.

In vivo Distribution Experiments

Fluorescence imaging and PA imaging were used to study the distribution of GNR@PEG-Qu at tumor sites in vivo. To observe the distribution of GNR@PEG-Qu in vivo, B16F10 tumor-bearing mice with 200–300 mm^3 tumor volume were randomly divided into two groups and administered PBS or GNR@PEG-Qu. Fluorescence imaging at different time points was performed with an IVIS spectroscopy system after administering the same dose of free Cy5.5 and Cy5.5 +GNR@PEG-Qu to the tail vein of mice. Twenty-four hours later, the mice were executed to remove their tumors and organs and analyze the fluorescence levels in the tissues. To perform PA imaging at the tumor site, B16F10 tumor-bearing mice were injected with GNR@PEG-Qu (5 mg/kg), and experiments were performed using a Vero LAIR animal PA and ultrasound imaging system. The excitation wavelength was 750 nm. The PA signal at the tumor site was recorded at 0, 1, 2, 3, 4, 8, 12, and 24 h.

Statistical Analysis

Statistical analysis was performed using GraphPad Prism software. All experimental data are presented as the mean ± S.E.M. Differences are considered statistically significant with *p < 0.05, **p < 0.01, and ***p < 0.001, ns, no significant difference.

Results and Discussion

Preparation and Characterization of GNR@PEG-Qu

Initially, gold nanorods were prepared using the seed-mediated growth method and were modified with SH-PEG_{5K}-COOH to obtain GNR@PEG. Finally, quercetin was loaded onto GNR@PEG by electrostatic adsorption to obtain GNR@PEG-Qu. The synthesis procedure of GNR@PEG-Qu is shown in Scheme 1. GNR@PEG are rod-like solid

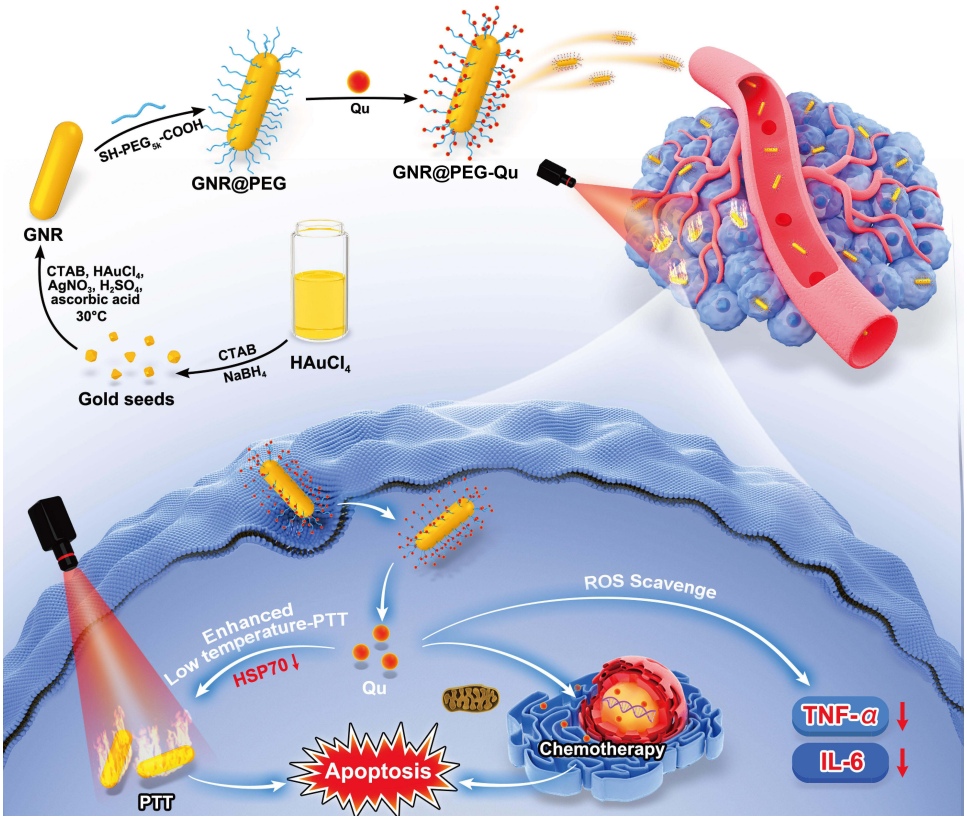

Scheme 1 Synthetic method and treatment strategy for melanoma using nanomedicine, including multifunctional treatment in vivo, enhancement of low-temperature PTT efficacy, and avoidance of oxidative stress.

nanoparticles with monodispersed particle size. The transmission electron microscopy (TEM) images of GNR@PEG-Qu in Figure 1a show that the sample exhibits a uniform rod-like morphology at approximately 200 nm. The UV-Vis absorption spectra of Qu, GNR@PEG, and GNR@PEG-Qu are shown in Figure 1b. It can be seen from the figure that the characteristic absorption peaks of GNR@PEG are at 1060nm and 530nm, and that of Qu are at 370nm. The two prepared GNR@PEG-Qu retain the typical absorption peaks of GNR@PEG and Qu respectively. This indicates the successful preparation of GNR@PEG-Qu and that coating Qu has no effect on the properties of GNR@PEG.In addition, GNR@PEG and GNR@PEG-Qu have wide absorption bond in the near infrared region, which indicates their ability to respond to NIR laser light. The particle size and zeta potential of GNR@PEG-Qu were determined by dynamic light scattering (DLS). The analysis showed that the particle size of GNR@PEG was approximately 218 nm, and the particle size of GNR@PEG after loading Qu was 247 nm (Figure 1c). The particle size of GNR@PEG-Qu is slightly larger than that of GNR@PEG, indicating the successful preparation of GNR@PEG-Qu. In addition, GNR@PEG in Figure 1d exhibits negative potentials, which is caused by the exposure of negatively charged -COOH after modification of GNR by SH-PEG$_{5K}$-COOH. The stronger negative potential of GNR@PEG-Qu is attributed to the negative potentials of GNR@PEG and Qu. This potential difference confirms that Qu was successfully attached to the GNR@PEG surface. Finally, the drug loading capacity of GNR@PEG-Qu was calculated to be 60.7%.

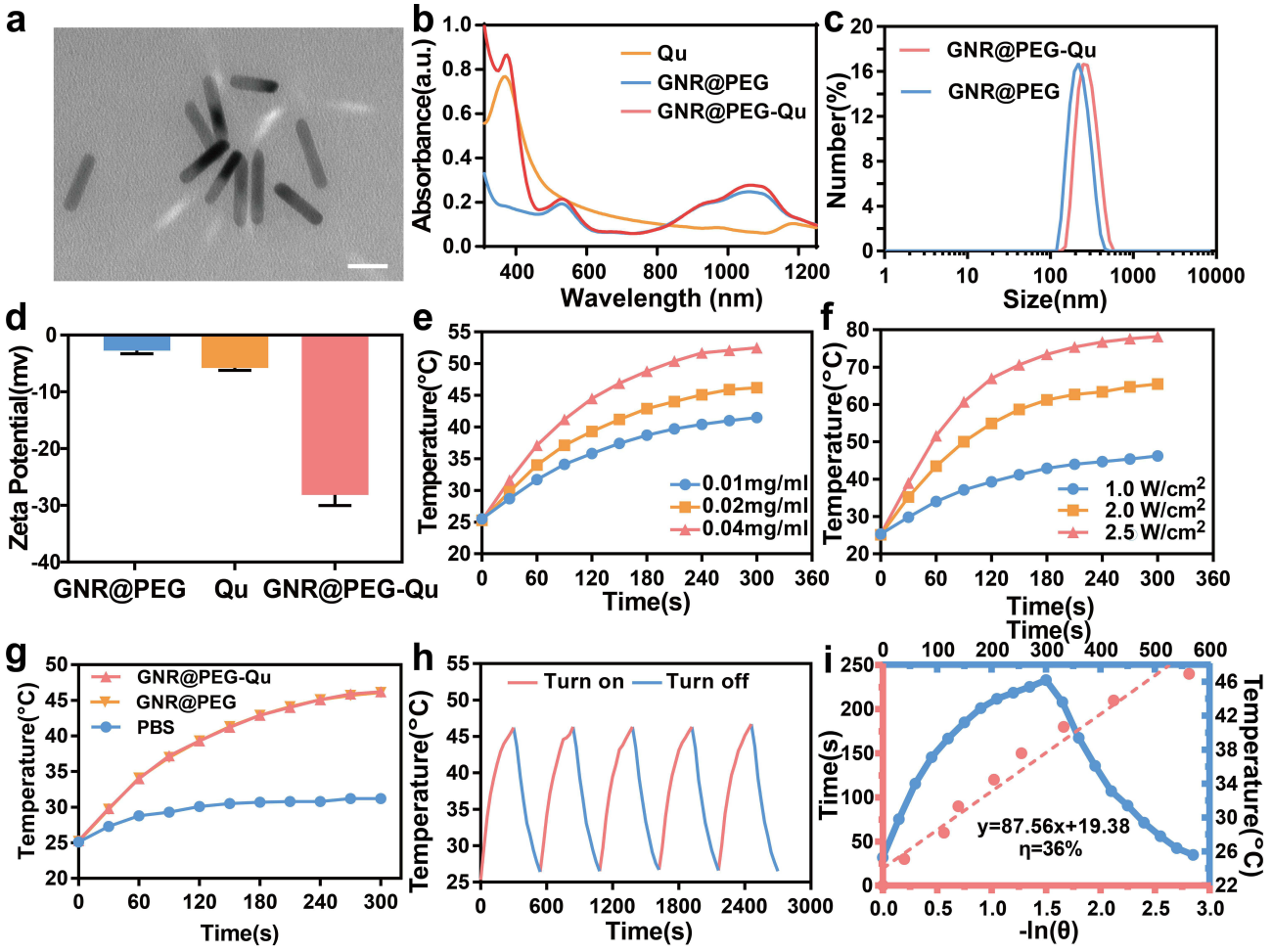

Figure 1 (**a**) Transmission electron microscopy (TEM) image of nanodrugs formed by loading quercetin on gold nanorods (GNR@PEG-Qu) (scale bar: 200 nm). (**b**) UV-Vis absorption spectra of Qu, GNR@PEG, and GNR@PEG-Qu in aqueous solution. (**c**) Dynamic light scattering (DLS) distribution and (**d**) zeta potential of GNR@PEG, Qu, and GNR@PEG-Qu. (**e**) Heat-up curves of different concentrations of GNR@PEG-Qu under laser irradiation. (**f**) Photothermal curves of GNR@PEG-Qu nanoparticles at different laser powers. (**g**) Photothermal curves of PBS, GNR@PEG, and GNR@PEG-Qu under irradiation. (**h**) Photothermal stability of GNR@PEG-Qu in aqueous solution under laser irradiation during five on/off cycles (irradiation: 1064 nm, 1.0 W/cm2). (**i**) Calculation of the photothermal conversion efficiency of GNR@PEG-Qu. The blue line represents one of the heating-cooling cycle curves of GNR@PEG-Qu; the red line represents the cooling time vs the negative natural logarithm of the temperature drive curve.

Subsequently, the photothermal properties of the GNR@PEG-Qu solution were investigated. The heat production efficiency of GNR@PEG-Qu was measured using an NIR thermal camera under 1064-nm NIR laser irradiation. The effects of irradiation time, concentration, and power intensity on the photothermal effect of GNR@PEG-Qu were first monitored. Figure 1e shows the concentration dependence of GNR@PEG-Qu. Samples of different concentrations were irradiated with a 1064 nm 1.0 W/cm^2 laser for 5 min, and it was found that the temperature of the samples increased as the concentration increased. The photothermal conversion ability of GNR@PEG-Qu was also affected by the laser power. As shown in Figure 1f, samples containing 0.02 mg/mL were irradiated by lasers with different powers, and the results showed that the higher the power, the more pronounced the rising temperature of GNR@PEG-Qu. Meanwhile, the temperature changes of phosphate buffered saline (PBS) and GNR@PEG-Qu were compared during 1064 nm 1.0 W/cm^2 laser irradiation for 5 min. After 1064-nm laser irradiation for 5 min, the temperature of GNR@PEG-Qu was significantly higher than that of PBS, and it continued to generate heat (Figure 1g). Figure S1 shows the photothermal visualization of the two materials, demonstrating a significant difference between the heat production capacity of PBS and GNR@PEG-Qu. Notably, the warming of GNR@PEG and GNR@PEG-Qu is consistent, indicating that the loading of Qu has no effect on the photothermal effect of GNR@PEG. These measurements show that GNR@PEG-Qu has a good photothermal effect, while GNR@PEG-Qu also has excellent photostability and achieves reproducible warming. Figure 1h shows that the temperature of GNR@PEG-Qu can be kept constant at 46.2 °C after five repeated on-off irradiation cycles of NIR irradiation, indicating its good photothermal stability, demonstrating the great potential of GNR@PEG-Qu for application in PTT. Finally, the photothermal conversion efficiency of GNR@PEG-Qu was quantified utilizing the η-value metric based on previously published calculations and was determined to be 36% through the cooling time of a photothermal cycle (Figure 1i), indicating favorable heat production by GNR@PEG-Qu under 1064-nm irradiation.

In vitro Cellular Uptake Assay and Anticancer Activity

Here, we chose the commonly used B16F10 cells to study the intracellular properties of GNR@PEG-Qu. Effective cellular uptake of nanoparticles will facilitate the tumor-killing effect of the drug. Therefore, we observed the cellular internalization and co-localization of GNR@PEG-Qu by confocal laser scanning microscopy (CLSM) and quantified the cellular uptake efficiency by flow cytometry. Primarily, Cy5.5-labeled GNR@PEG-Qu was incubated with B16F10 cells for 1, 3, and 6 h. The cell nuclei were stained with Hoechst 33342. GNR@PEG-Qu co-localized with the nucleus at different time points, and the position of GNR@PEG-Qu could be clearly visualized. The uptake process shown in Figure 2a and Figure S2 are time-dependent, with the fluorescence intensity becoming stronger with increasing time. Flow cytometry was employed to quantify the cellular uptake results in Figure 2b consistent with CLSM.

To determine the potential toxicity of GNR@PEG-Qu on B16F10 cells, the effects of different concentrations of GNR@PEG-Qu and laser irradiation on the viability of B16F10 cells were measured using a standard CCK-8 cytotoxicity assay. The survival rate of B16F10 cells after 24 h of incubation in GNR@PEG-Qu (at concentrations of 0, 50, 100, 200, and 400 μg/mL, respectively) is shown in Figure 2c. The results show that a low concentration of GNR@PEG-Qu has little toxicity to cells. Mild toxicity was observed at concentrations up to 100 μg/mL, and cell survival was >80%. As the concentration of Qu increased to 400 μg/mL, the cell viability decreased to less than 50%. Only high concentrations of GNR@PEG-Qu caused significant cytotoxicity, indicating that the nanodrugs are biocompatible. With irradiation with NIR light (1064 nm, 1.0 W/cm^2, 1 min), GNR@PEG-Qu increased the incubation temperature of the cells from 37 °C to 45 °C, exerting a mild PTT effect. The results suggest that PTT combined with chemotherapy resulted in reduced cell survival, and this synergistic effect enhanced the treatment of cancer cells with GNR@PEG-Qu. In order to visualize the synergistic ability of GNR@PEG-Qu, the combination index (CI) was calculated to express that the nanomedicine has a 1+1 > 2 effect on melanoma treatment. Therefore, CI of 0.906 was calculated using the experimental results of CCK8, further demonstrating that GNR@PEG-Qu has a synergistic therapeutic effect. Cytotoxicity was further observed using live/dead staining and cytotoxicity assays. Cells treated with different formulations were labeled with Calcein-AM (acetoxymethyl) and propidium iodide (PI) to identify living and dead cells, respectively. The results revealed no significant cell death in the unilluminated GNR@PEG and PBS groups under 1064-nm illumination, as shown in Figure 2d and Figure S3, indicating the relative safety of 1064-nm laser and GNR@PEGs to cells. Compared to PBS

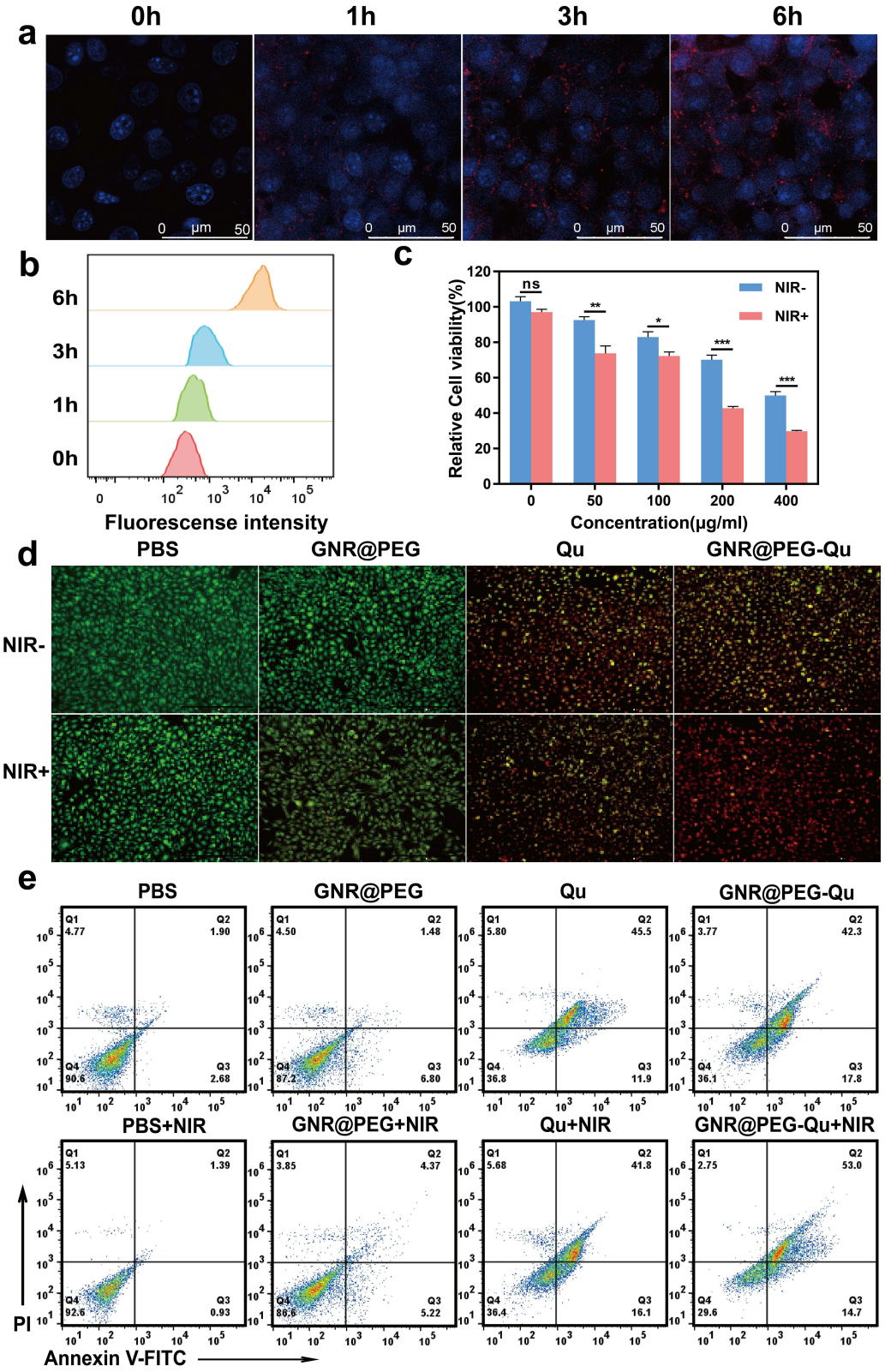

Figure 2 (**a**) Confocal laser scanning microscopy (CLSM) images showing the uptake of Cy5.5-labeled GNR@PEG-Qu in B16F10 cells at different time points; scale bar: 50 μm. (**b**) Evaluation of the uptake of Cy5.5-labeled GNR@PEG-Qu by B16F10 cells at different time points using flow cytometry. (**c**) Cell viability at different concentrations of GNR@PEG-Qu under dark or 1064-nm laser irradiation conditions was assessed by the CCK-8 method (*$p < 0.05$, **$p < 0.01$, and ***$p < 0.001$, ns, no significant difference). (**d**) Apoptosis level of B16F10 cells in different formulation groups evaluated using Calcein-AM and PI staining, scale bar: 400 μm. (**e**) Apoptosis of different groups of cells was analyzed by flow cytometry.

in the dark, GNR@PEG+NIR resulted in increased cell death and more pronounced red fluorescence of Qu, confirming the PTT of GNR@PEG and the chemotherapeutic effect of Qu. GNR@PEG-Qu+NIR showed all-red fluorescence with negligible green fluorescence, indicating cell death. Therefore, GNR@PEG-Qu has a satisfactory killing effect on B16F10 cells.

In addition, Annexin V has a great affinity for phosphatidylserine during apoptosis; therefore, the role of GNR@PEG-Qu (100 μg/mL) with the presence of 1064-nm light inducing cell death was investigated by co-labeling with Membrane Linkin V-Fluorescein Isothiocyanate (Annexin V-FITC) and PI. The inhibition rates of cells by chemotherapy alone and PTT alone were used as controls. The flow cytometry results shown in Figure 2e demonstrate that the percentage of apoptotic cells after 1064 nm, 1.0 W/cm^2, 5 min laser irradiation was approximately 67.7%, which was higher than the percentage of apoptotic cells after 37 °C control (2.58%), Qu (57.4%), GNR@PEG-Qu group treatment (60.1%), and GNR@PEG light alone (9.59%). Combined PTT and chemotherapy treatment with GNR@PEG-Qu significantly promoted the apoptosis of B16F10 cells. These results suggest that GNR@PEG-Qu is an effective synergistic anticancer agent and that chemotherapy treatment with GNR@PEG-Qu combined with PTT is superior to chemotherapy alone or PTT alone.

In vitro Hsp70 Inhibition and Oxidative Stress Avoidance

Hsp70 is a key Hsp in mammalian cells, which enables cancer cells to resist temperature-induced apoptosis in PTT and makes PTT less effective. Therefore, effective inhibition of Hsp70 expression in PTT therapy promotes cell killing. Qu has been reported as a promising Hsp70 inhibitor in previous studies. The combination of GNR@PEG and Qu in this study cleverly exploited this by reducing Hsp70 expression to promote the photothermal effects of GNR@PEG during low-temperature PTT. The protein expression was evaluated to verify the mechanism by which Qu inhibits Hsp70 and thus sensitizes PTT. The results showed that GNR@PEG-Qu could inhibit the expression of Hsp70 under hypothermic conditions. Hsp70 expression in B16F10 cells of GNR@PEG-Qu under different treatments was analyzed by Western blotting, as shown in Figure 3a. After laser light irradiation, Hsp70 expression was upregulated in the GNR@PEG group, which was higher than that in the group that was not subjected to NIR light irradiation, indicating the occurrence of PTT. Hsp70 expression was significantly reduced when Qu was combined with GNR@PEG, suggesting that Qu could downregulate Hsp70 to inhibit the heat resistance of cancer cells, which provides a great possibility for the efficient treatment of PTT. Semi-quantitative analysis of the Western blotting results in Figure 3b demonstrates consistent results.

Numerous previous studies have shown an important link between melanoma formation and high levels of ROS expression and oxidative stress. Increased levels of ROS contribute to melanoma development and drug resistance. Therefore, inhibiting the increase in ROS levels by suppressing the antioxidant response in melanoma cells would be beneficial for treatment. It has been shown that Qu has antioxidant properties and can reduce ROS levels;[65] this has also been confirmed in the report of Rafiq et al.[46] In this study, to investigate the antioxidant effect of GNR@PEG-Qu on B16F10 cells, we detected ROS generation using the fluorescent dye DCFH-DA (Figure 3c). First, the cells were induced to produce significant ROS using H_2O_2, before incubating the cells with Qu and GNR@PEG-Qu. Due to the antioxidant properties, the expression of ROS was reduced compared to that in control cells, whereas the laser-irradiated NIR group expressed higher levels of ROS due to PTT-induced oxidation. This result reflects the excellent ROS scavenging ability of GNR@PEG-Qu.

In vivo Imaging

Poor drug accumulation and systemic toxicity limit the efficacy of drugs against tumors. Adequate drug accumulation at the tumor site is an important method of improving efficacy. Therefore, we conducted a tumor biodistribution study of GNR@PEG-Qu in mice before investigating its antitumor efficacy. Cy5.5 is an outstanding dye in in vivo fluorescence imaging. To study the accumulation of GNR@PEG-Qu in organisms, Cy5.5-labeled GNR@PEG-Qu (Cy5.5 +GNR@PEG-Qu) was injected intravenously, and fluorescent images at different time intervals were captured using an IVIS system. Fluorescence imaging at different time points (0, 1, 2, 4, 8, 12, and 24 h) after drug injection into the tail vein of mice is shown in Figure 4a. The fluorescence intensity of the tumor sites in different groups can be seen in the figure After drug administration, the fluorescence intensity of the tumor site in the free Cy5.5 group first increased

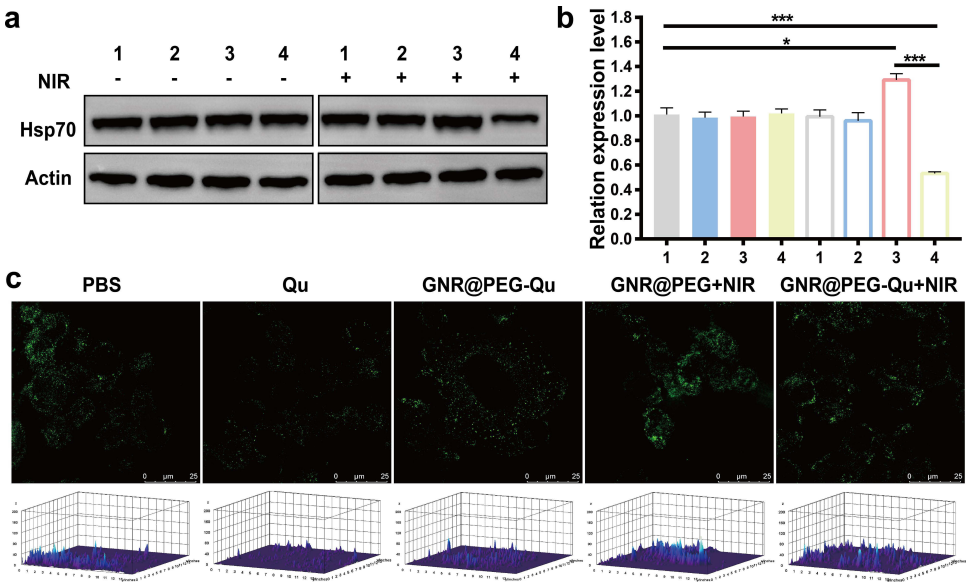

Figure 3 (**a**) The expression level of intracellular Hsp70 in B16F10 cells after incubation with different formulations was assessed by Western blot, with GADPH as an internal reference (1: PBS, 2: Qu, 3: GNR@PEG, 4: GNR@PEG-Qu). (**b**) Quantified relative expression level of Hsp70 in the Western blot image (*$p < 0.05$ and ***$p < 0.001$). (**c**) ROS expression in different groups after H_2O_2 pretreatment of cells. The fluorescence image taken by CLSM is on top, and below it is the quantitative analysis of fluorescence intensity; scale: 25 nm.

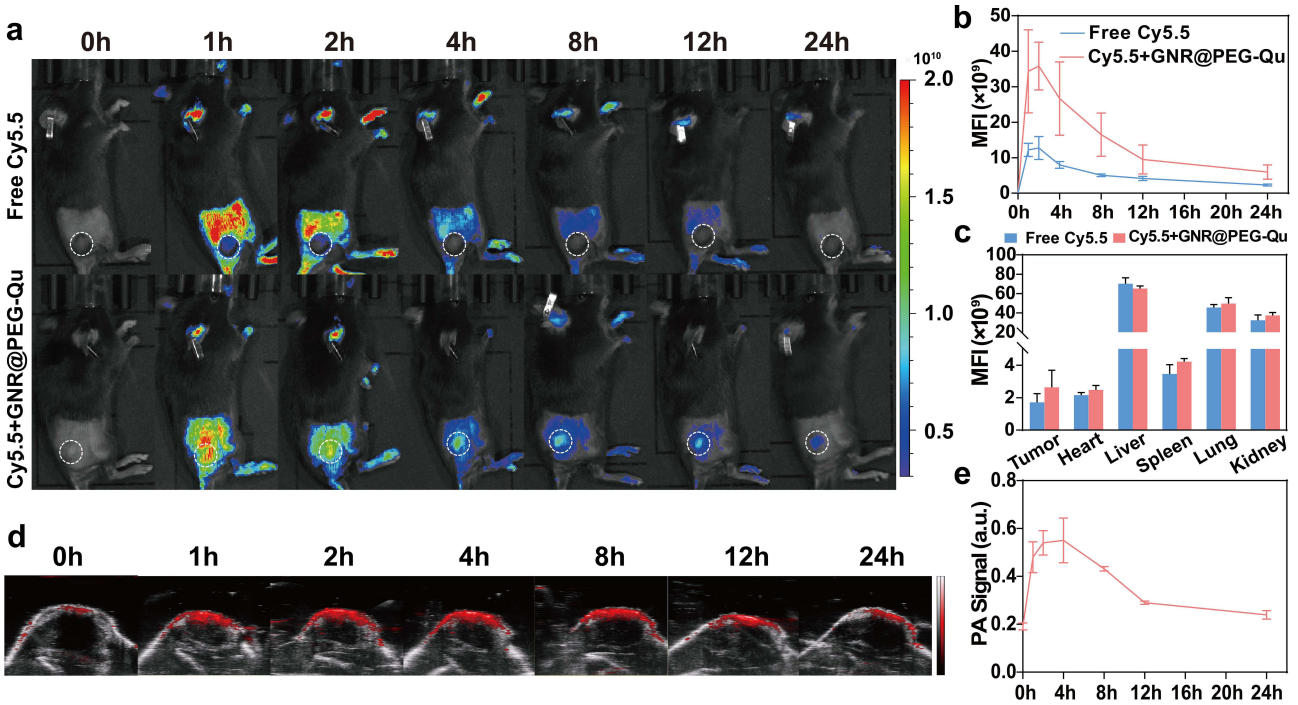

Figure 4 (**a**) Fluorescence imaging in vivo of mice at different time points after injection of Cy5.5 and Cy5.5+GNR@PEG-Qu. (**b**) Quantitative analysis of the average fluorescence intensity at the tumor site. (**c**) Quantitation of the mean fluorescence intensity in each group of tumors and major organs (n = 5). (**d**) Photoacoustic (PA) imaging demonstrating the accumulation of GNR@PEG-Qu in mouse tumor sites. (**e**) Change curve of the PA signal intensity at different time points.

continuously and then the fluorescence disappeared rapidly, indicating that free Cy5.5 would be metabolized rapidly by mice. In contrast, compared to free Cy5.5, the fluorescence of the Cy5.5+GNR@PEG-Qu group was clearly visible at 24 h, indicating a significant accumulation of the drug at the tumor site. The higher fluorescence intensity of the administered group compared to the control group at all time intervals can be clearly seen in the analysis of the average

fluorescence intensity in Figure 4b, again illustrating the accumulation of GNR@PEG-Qu at the tumor site. In conclusion, the fluorescence imaging in mice showed that GNR@PEG-Qu had a significant improvement in tumor tissue delivery efficiency and enrichment time at the tumor site compared with free Cy5.5. Finally, major organs and tumors were excised 24 h after injection, and the fluorescence intensity was measured. As can be seen in Figure S4, the fluorescence signals of the heart and spleen were weaker in the different formulation groups, indicating that GNR@PEG-Qu was less toxic to these two organs. Figure 4c shows the average fluorescence intensity of the tumor and major organs. As mentioned in the previous results, the fluorescence intensity of tumors in the administered group was greater than that in the control group. In addition, the fluorescence intensities of major organs in the two groups were not significantly different, indicating that GNR@PEG-Qu does not cause serious damage to organisms and ensures a certain degree of biosafety. These results suggest that GNR@PEG-Qu can effectively accumulate at the tumor site, thus maximizing the anti-tumor effect and minimizing side effects.

Photoacoustic (PA) imaging of GNR@PEG-Qu was investigated in vivo because of the strong NIR absorbance of gold nanoparticles, which can be used as a contrast agent for PA imaging (Figure 4d). In vivo PA images of B16F10 tumor-bearing mice were captured at different time points after administration of GNR@PEG-Qu (100 μL) into the tail vein. Under 750-nm excitation, the PA signal was clearly visible at the tumor site, and the signal value reached the maximum at 4 h. The intensity was enhanced 2.88-fold compared to the control group (Figure 4e). This result is consistent with the conclusion of in vivo fluorescence imaging, both demonstrating that GNR@PEG-Qu has good accumulation at the tumor site. The PA results demonstrate the potential of GNR@PEG-Qu as a PA imaging contrast agent, allowing more accurate imaging to guide cancer treatment.

In vivo Antitumor Therapy

To evaluate the antitumor potential of GNR@PEG-Qu in vivo, its therapeutic effect was investigated using C57BL/6 mice. Figure 5a completely depicts the exploration of the therapeutic effect of GNR@PEG-Qu on B16F10-bearing mice. B16F10 cells were first injected subcutaneously into the right side of the mice above the leg to cause the tumor to grow. Five days later, when the tumor volume reached approximately 100 mm^3, mice were randomly divided into five groups (n = 5) and injected with 100 μL of various preparations in the tail vein, including (1) PBS, (2) Qu, (3) GNR@PEG-Qu, (4) GNR@PEG+NIR, and (5) GNR@PEG-Qu+NIR. Qu was administered at a dose of 5 mg/kg, and GNR@PEG was administered at a dose of 1 mg/kg. For the NIR laser irradiation group, 1064-nm laser irradiation was performed after drug administration for 4 h. After 16 days of treatment, the main organs and tumor tissues of mice were obtained for further analysis to determine whether GNR@PEG-Qu could effectively inhibit tumor growth. First, the photothermal effect in vivo was evaluated. The temperature changes in the tumor regions of B16F10 tumor-bearing mice under different treatment modalities were recorded by infrared thermography, and the results are shown in Figure 5b, including PBS, GNR@PEG, and GNR@PEG-Qu. After 8 h of drug injection, the tumor-bearing mice were anesthetized and irradiated with a 1064 nm, 1.5 W/cm^2 NIR laser. The temperature changes at the tumor site in PBS-injected mice were not significant after 300 s of laser irradiation. In contrast, the temperature of GNR@PEG-Qu treated mice increased rapidly from ~33.2 °C to 44.3 °C, which met the requirements for mild PTT and was sufficient for thermotherapy-induced tumor ablation. The warming histogram of GNR@PEG was similar to that of GNR@PEG-Qu, indicating that the photothermal effect of GNR@PEG in vivo remained unaffected by Qu. These results suggest that GNR@PEG-Qu is effective in converting light into heat therapy in vivo.

The in vivo antitumor effects of nanoparticles were further investigated. The mice were administered different formulations and the light groups were irradiated with a laser. The tumor volume and body weight of the mice were subsequently recorded over the next 16 days. Figure 5c shows the change in the tumor volume after treatment. Compared to the PBS group, the GNR@PEG+NIR group could not effectively inhibit tumor growth, which was related to the mild photothermal effects demonstrated by GNR@PEG. In contrast, free Qu and GNR@PEG-Qu showed some therapeutic effects, and the tumor volume was obviously smaller than that of the PBS group, which was attributed to the chemotherapeutic effect of Qu. Under light irradiation, the anti-tumor effect of the GNR@PEG-Qu+NIR group was significant, and the difference in tumor volume between the two groups was statistically significant compared to that observed in the PBS group. This suggests that combined mild PTT and chemotherapy treatment has an excellent effect.

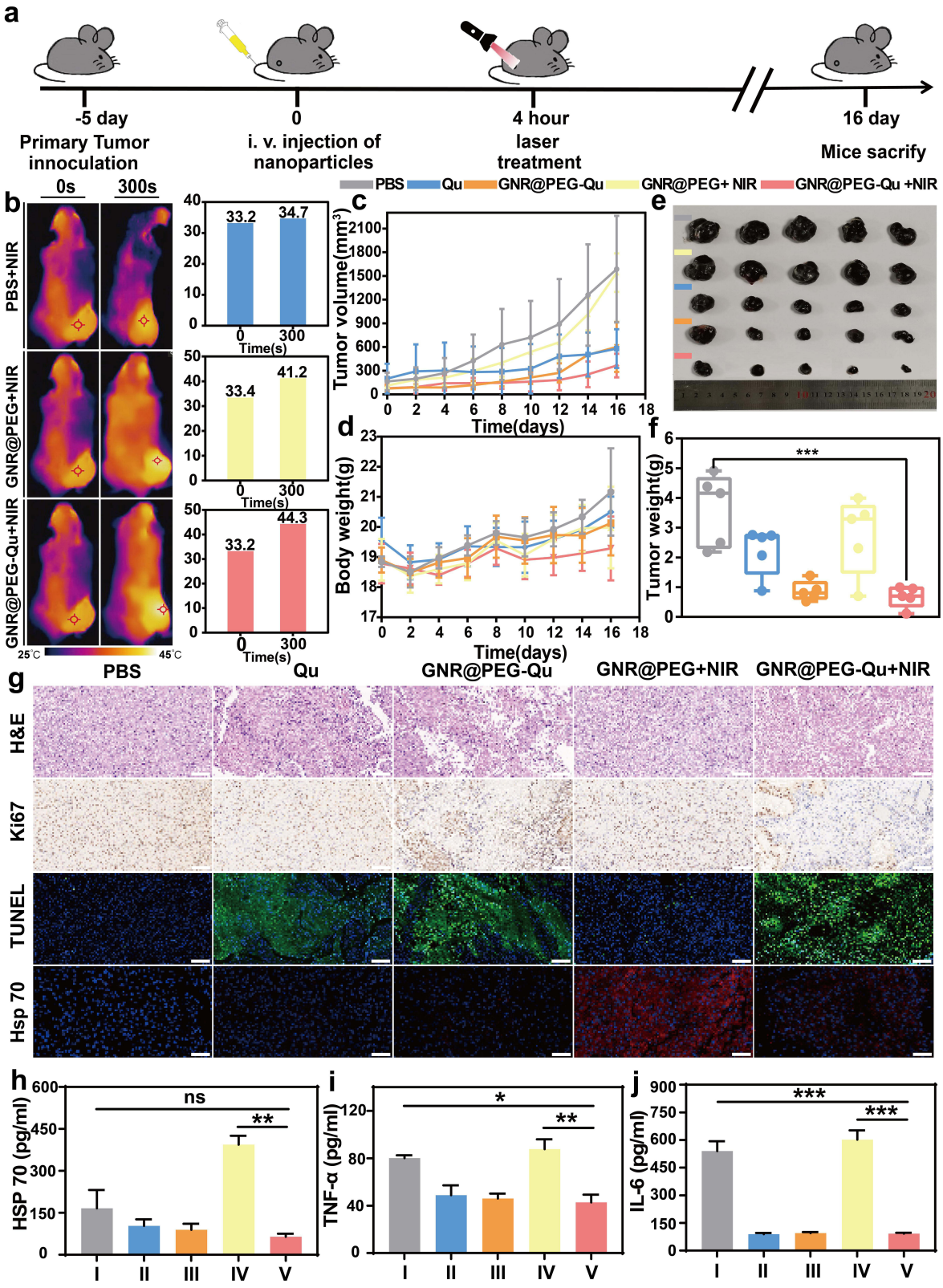

Figure 5 (**a**) Timeline of the treatment of melanoma by GNR@PEG-Qu. (**b**) Photothermal images of tumor sites in mice with different dosing groups (PBS, GNR@PEG, GNR@PEG-Qu) during laser irradiation. The bar chart on the right shows the temperature change after 300 s of irradiation. (**c**) Changes in tumor volume in different formulation groups (PBS, Qu, GNR@PEG-Qu, GNR@PEG+NIR, and GNR@PEG-Qu+NIR). (**d**) Changes in the average body weight of mice in each group during the 16-day treatment period. (**e**) Photograph of tumor tissues from different treatment groups. (**f**) Excised tumor weight of different groups (***$p < 0.001$). (**g**) Histological analysis of tumors from different dosing groups, including H&E, Ki67, and TUNEL staining; scale bar: 200 μm. The last row shows the immunofluorescence images of Hsp70 staining in different groups of tumor sections. The Hsp70 expression region was stained with Hsp70 antibody (red), and the nucleus was stained with DAPI (blue). Scale bar: 50 μm. (**h**–**j**) The serum levels of Hsp70, TNF-α, and IL-6 in mice were measured after 16 days of treatment. (**I**) PBS; II: Qu; III: GNR@PEG-Qu; IV: GNR@PEG+NIR; (**V**) GNR@PEG-Qu+NIR (*$p < 0.05$, **$p < 0.01$, and ***$p < 0.001$, ns, no significant difference).

Figure 5d shows the change in body weight of the mice during the 16-day treatment period. Although the mice were administered different formulations, their weight continued to increase, and there was no significant difference between the groups, demonstrating that the side effects of GNR@PEG-Qu were minimal. Figure S5 shows representative photographs of B16F10 tumor-bearing mice from each treatment group. No obvious burns were observed in the photographs of the mice after the tumor sites were irradiated by the laser, indicating that the mild photothermal treatment caused no damage to normal tissues and had a good safety profile. Tumors removed 16 days after treatment were photographed (Figure 5e) and weighed (Figure 5f). The excellent tumor growth inhibition effect of the GNR@PEG-Qu +NIR group was demonstrated by these results. Subsequently, the biosafety and antitumor activity of GNR@PEG-Qu were further confirmed. Mice were executed, and tumors and major organs were removed at the end of the 16 days of treatment monitoring. Tumors and organs were analyzed using histological methods, and the results are shown in Figure 5g. The results of H&E, TUNEL, and Ki-67 staining showed that different treatment groups showed different degrees of tumor damage, which was manifested as cell shrinkage, nuclear chromatin condensation, and fragmentation. Among them, the B16F10 cells of GNR@PEG-Qu+NIR had more apoptotic cells and less proliferating cells, demonstrating that GNR@PEG-Qu inhibited B16F10 tumor growth in vivo. Among the various treatments, the GNR@PEG-Qu +NIR group had the most severe tumor damage, indicating that the GNR@PEG-Qu+NIR group had the best anti-tumor effect.

In vivo Hsp70 Inhibition and Oxidative Stress Avoidance

According to the results of previous studies, GNR@PEG-Qu can alleviate heat resistance in cancer cells by inhibiting Hsp70 expression. Therefore, the expression level of Hsp70 in tumor tissues of mice in different treatment groups was determined in in vivo assays. Immunofluorescence staining results shown in Figure 5g indicated that the difference was significant. As expected, the expression of Hsp70 in the tumors of GNR@PEG+NIR-treated mice was significantly higher than that in the PBS group. The experimental results were consistent with the conclusion that Hsp70 is highly expressed in low-temperature PTT and that it reduces the therapeutic effect of PTT. In contrast, the expression of Hsp70 in tumor tissues of GNR@PEG-Qu+NIR-treated mice was significantly reduced, indicating that GNR@PEG-Qu downregulated the expression of Hsp70 in tumor tissues. Subsequently, we detected the Hsp70 levels in mouse serum using an enzyme-linked immunosorbent assay (ELISA) kit, and the results shown in Figure 5h were consistent with the immunofluorescence staining results described above. After laser irradiation, the level of HSP70 in the tumor site increased significantly. Treatment with GNR@PEG-Qu significantly downregulated its expression level, even with no significant difference from the control group. The results of the in vivo experiment indicate that GNR@PEG-Qu can effectively downregulate the expression of Hsp70 in tumors, thereby significantly reducing the thermal resistance of cancer cells, thus enabling low-temperature PTT to have a good tumor ablation effect.

The presence of ROS in melanoma and the large amount of ROS generated during PTT treatment represent a potential threat by promoting tumor growth and causing irreversible damage to surrounding normal cells and tissues. When excessive hydrogen peroxide (H_2O_2) is produced in an organism, macrophages are stimulated to produce large amounts of tumor necrosis factor α (TNF-α) and trigger severe inflammation. Therefore, the serum levels of inflammatory factors were measured to assess the anti-inflammatory activity of GNR@PEG-Qu. As shown in Figure 5i and j, the GNR@PEG+NIR group showed an increase in the expression levels of TNF and IL-6 due to laser irradiation, indicating that ROS induced inflammation. In contrast, the levels of inflammatory factors were significantly reduced when Qu was added. The expression of inflammatory factors was also significantly suppressed compared to the control group. Specifically, the GNR@PEG-Qu+NIR group exhibited significantly reduced expression of inflammatory factors, suggesting that ROS-induced inflammation was effectively suppressed in vivo.

Systemic Biological Safety of GNR@PEG-Qu

Finally, the biological safety of GNR@PEG-Qu was assessed. The heart, liver, spleen, lungs, and kidneys were obtained from mice executed on day 16 for histological analysis. No significant pathologic abnormalities were found in organ sections of the treatment group compared to those of the control group, indicating that none of the

treatments caused significant toxicity to major organs (Figure 6a). To fully consider the safety of GNR@PEG-Qu in vivo, blood analyses were performed on live mice after 16 days of treatment (Figure 6b and c). Additionally, there was no significant difference in the expression of liver and kidney function markers in GNR@PEG-Qu+NIR-treated mice compared to control mice, indicating that the drug has no systemic side effects. The above results indicate that GNR@PEG-Qu has good safety and good antitumor effects on normal organs by PTT combined with chemotherapy.

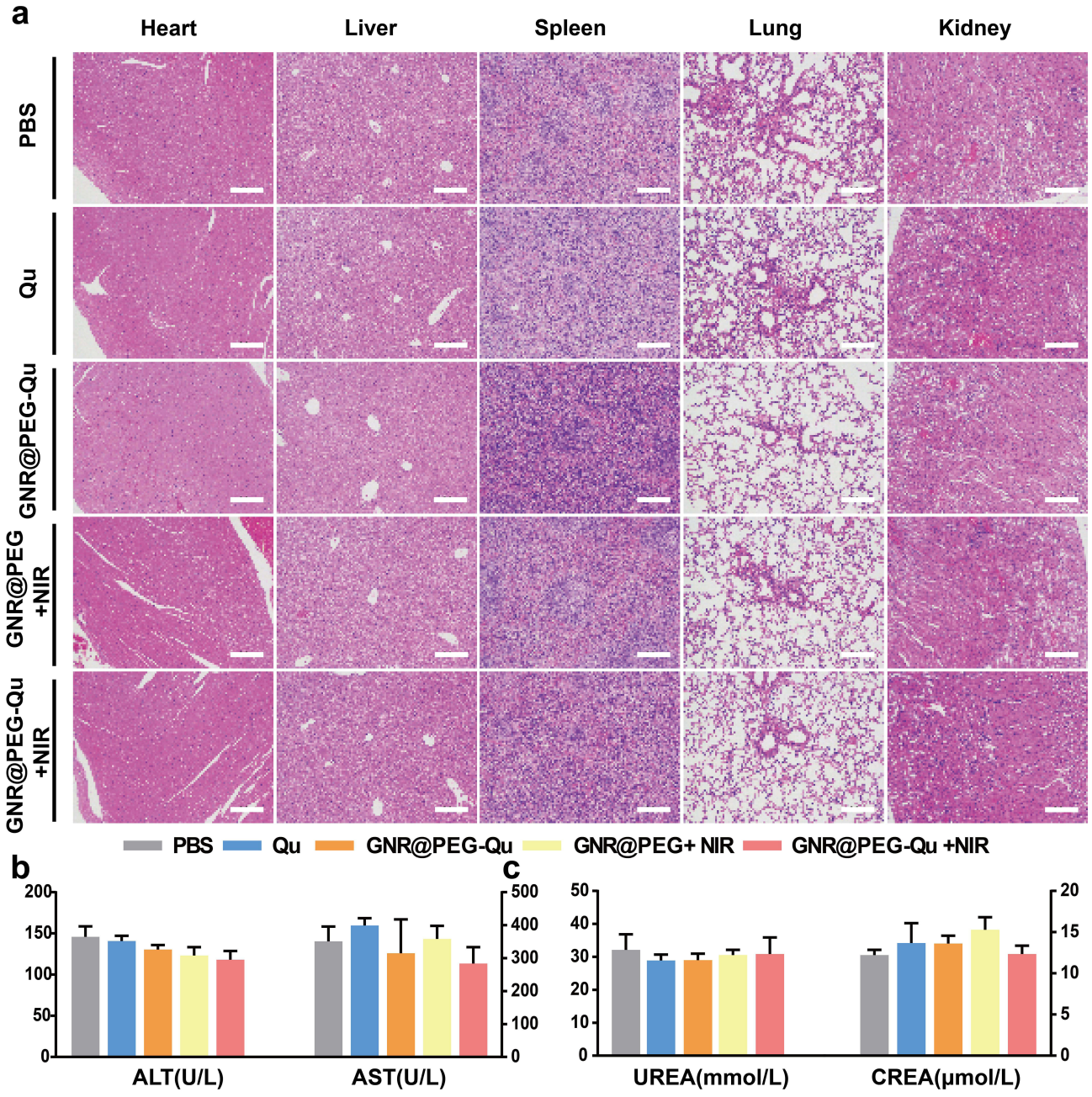

Figure 6 (**a**) H&E staining of major organ sections from different groups of mice (PBS, Qu, GNR@PEG-Qu, GNR@PEG+NIR, and GNR@PEG-Qu+NIR). (**b** and **c**) Biochemical analysis of liver and kidney indexes in the serum of mice after injection of different formulas through the tail vein.

Conclusion

In this study, we successfully prepared a multifunctional nanosystem for the treatment of melanoma. The nanosystem significantly inhibited the growth of B16F10 melanoma cells in vivo and in vitro by low-temperature PTT synergistic chemotherapy. Meanwhile, Qu inhibited the expression of ROS at the tumor site and balanced redox homeostasis to further improve the treatment of melanoma. In summary, GNR@PEG-Qu is a nanomedicine with multifunctionality that integrates PTT, chemotherapy, ROS scavenging, and oxidative stress avoidance effects, which provides a new perspective for the treatment of melanoma.

Acknowledgments

This work was supported by Natural Science Foundation of Guangdong Province (2024A1515030063, 2022A1515011337), Guangdong Province Universities and Colleges Characteristic Innovation (2021KTSCX036), Traditional Chinese Medicine Research Project of Guangdong Province Traditional Chinese Medicine Bureau (20221206), Discipline Construction Project of Guangdong Medical University (4SG24015G), Construction Project of Nano Technology and Application Engineering Research Center of Guangdong Medical University (4SG24179G) and Funds for PHD researchers of Guangdong Medical University in 2024. We thank LetPub (www.letpub.com) for its linguistic assistance during the preparation of this manuscript.

Disclosure

The authors report no conflicts of interest in this work.

References

1. Schadendorf D, Van Akkooi ACJ, Berking C, et al. Melanoma. *Lancet*. 2018;392(10151):971. doi:10.1016/s0140-6736(18)31559-9
2. Long GV, Swetter SM, Menzies AM, et al. Cutaneous melanoma. *Lancet*. 2023;402(10400):485. doi:10.1016/s0140-6736(23)00821-8
3. Franke V, Van Akkooi ACJ. The extent of surgery for stage III melanoma: how much is appropriate? *Lancet Oncol*. 2019;20(3):167. doi:10.1016/s1470-2045(19)30099-3
4. Yue J, Vendramin R, Liu F, et al. Targeted chemotherapy overcomes drug resistance in melanoma. *Genes Dev*. 2020;34(9–10):637. doi:10.1101/gad.333864.119
5. Mitchell MS, Clin J. Chemotherapy for melanoma: the resultant of conflicting vectors. *Oncol*. 2004;22(11). doi:10.1200/jco.2004.03.976
6. Bhave P, Hong A, Lo SN, et al. Efficacy and toxicity of adjuvant radiotherapy in recurrent melanoma after adjuvant immunotherapy. *J Immunother*. 2023;11(3). doi:10.1136/jitc-2022-006629
7. Wang L, Shen KZ, Gao X, et al. Melanoma derived exosomes amplify radiotherapy induced abscopal effect via IRF7/I-IFN axis in macrophages. *Adv Sci*. 2024;11(13). doi:10.1002/advs.202304991
8. Carvajal RD, Sacco JJ, Jager MJ, et al. Advances in the clinical management of uveal melanoma. *Nat Rev Clin Oncol*. 2023;20(2):99. doi:10.1038/s41571-022-00714-1
9. Seth R, Messersmith H, Kaur V, et al. Systemic therapy for melanoma: ASCO guideline. *J Clin Oncol*. 2020;38(33):3947–3970. doi:10.1200/jco.20.00198
10. Arslanbaeva LR, Santoro MM. Adaptive redox homeostasis in cutaneous melanoma. *Redox Biol*. 2020;37:101753. doi:10.1016/j.redox.2020.101753
11. Zhang X, Gibhardt CS, Will T, et al. Redox signals at the ER –mitochondria interface control melanoma progression. *EMBO J*. 2019;38(15):100871. doi:10.15252/embj.2018100871
12. Castejón-Griñán M, Cerdido S, Sánchez-Beltrán J, et al. Melanoma-associated melanocortin 1 receptor variants confer redox signaling-dependent protection against oxidative DNA damage. *Redox Biol*. 2024;71:103135. doi:10.1016/j.redox.2024.103135
13. Cannavò SP, Tonacci A, Bertino L, et al. The role of oxidative stress in the biology of melanoma: a systematic review. *Res Pract*. 2018;215:21. doi:10.1016/j.prp.2018.11.020
14. Liu Y, Bhattarai P, Dai Z, et al. Photothermal therapy and photoacoustic imaging via nanotheranostics in fighting cancer. *Chem Soc Rev*. 2018;7:1855. doi:10.1039/c8cs00618k
15. de Melo-Diogo D, Pais-Silva C, Dias DR, et al. Strategies to improve cancer photothermal therapy mediated by nanomaterials. *Adv Healthc Mater*. 2017;6(10):1700073. doi:10.1002/adhm.201700073
16. Huang X, Lu Y, Gao M, et al. Recent strategies for nano-based PTT combined with immunotherapy: from a biomaterial point of view. *Theranostics*. 2021;11(15):7546. doi:10.7150/thno.56482
17. Du B, Ma C, Ding G, et al. Cooperative strategies for enhancing Performance of Photothermal Therapy (PTT) agent: optimizing its photothermal conversion and cell internalization ability. *Small*. 2017;13(13):1603275. doi:10.1002/smll.201603275
18. Cui X, Ruan Q, Zhuo X, et al. Photothermal nanomaterials: a powerful light-to-heat converter. *Chem Rev*. 2023;123(11):6891. doi:10.1021/acs.chemrev.3c00159
19. Zhi D, Yang T, O'Hagan J, et al. Photothermal therapy. *J Control Release*. 2020;325:52. doi:10.1016/j.jconrel.2020.06.032
20. Liu S, Pan X, Liu H. Two-dimensional nanomaterials for photothermal therapy. *Angew Chem Int Ed*. 2020;59(15):5890. doi:10.1002/anie.201911477

21. Wu Y, Yao Y, Zhang J, et al. Tumor-targeted injectable double-network hydrogel for prevention of breast cancer recurrence and wound infection via synergistic photothermal and brachytherapy. *Adv Sci*. 2022;9(24):2200681. doi:10.1002/advs.202200681
22. Xu Q, Wan J, Bie N, et al. A biomimetic gold nanocages-based nanoplatform for efficient tumor ablation and reduced inflammation. *Theranostics*. 2018;8(19):5362. doi:10.7150/thno.27631
23. Wu J, Yin H, Song X, et al. Vanadium carbide Mxenzyme harnessing photothermal effects for targeted lung tumor suppression and inflammation eradication. *Adv Funct Mater*. 2024;34(18):2313997. doi:10.1002/adfm.202313997
24. Ding B, Shao S, Jiang F, et al. MnO_2 -disguised upconversion hybrid nanocomposite: an ideal architecture for tumor microenvironment-triggered UCL/MR bioimaging and enhanced chemodynamic therapy. *Chem Mater*. 2019;31(7):2651. doi:10.1021/acs.chemmater.9b00893
25. Chang M, Wang M, Hou Z, et al. Problems and solutions of nanomaterials in antitumor photothermal therapy. *Chin J Lumin*. 2022;43(7):995. doi:10.37188/cjl.20220118
26. Yang K, Zhao S, Li B, et al. Low temperature photothermal therapy: advances and perspectives. *Coord Chem Rev*. 2021;454:214330. doi:10.1016/j.ccr.2021.214330
27. Yi X, Duan Q, Wu F. Low-temperature photothermal therapy: strategies and applications. *Research*. 2021;2021:9816594. doi:10.34133/2021/9816594
28. Tian B, Wang C, Du Y, et al. Near infrared-triggered theranostic nanoplatform with controlled release of HSP90 inhibitor for synergistic mild photothermal and enhanced nanocatalytic therapy with hypoxia relief. *Small*. 2022;18(28):2200786. doi:10.1002/smll.202200786
29. Ding Z, Gu Y, Zheng C, et al. Organic small molecule-based photothermal agents for cancer therapy: design strategies from single-molecule optimization to synergistic enhancement. *Coord Chem Rev*. 2022;464:214564. doi:10.1016/j.ccr.2022.214564
30. Ma W, Sun R, Tang L, et al. Bioactivable STING nanoagonists to synergize NIR-II mild photothermal therapy primed robust and long-term anticancer immunity. *Adv Mater*. 2023;35(48):2303149. doi:10.1002/adma.202303149
31. Li K, Xu K, Liu S, et al. Multienzyme-like Reactivity cooperatively impairs glutathione peroxidase 4 and ferroptosis suppressor protein 1 pathways in triple-negative breast cancer for sensitized ferroptosis therapy. *ACS Nano*. 2023;17(20):20218. doi:10.1021/acsnano.1c08664
32. Ding X, Wang T, Bai S, et al. A dual heat shock protein down-regulation strategy using PDA/Cu/ICG/R controlled by NIR "switch" enhances mild-photothermal therapy effect. *Adv Healthcare Mater*. 2023;12(27):2300929. doi:10.1002/adhm.202300929
33. Ma G, Liu Z, Zhu C, et al. H_2O_2 -responsive NIR-II AIE nanobomb for carbon monoxide boosting low-temperature photothermal therapy. *Angew Chem Int Ed*. 2022;61(36):e202207213. doi:10.1002/anie.202207213
34. Sun Z, Li T, Wu F, et al. Precise synergistic photothermal therapy guided by accurate temperature-dependent NIR-II fluorescence imaging. *Adv Funct Mater*. 2023;34(14):2311622. doi:10.1002/adfm.202311622
35. Tong F, Hu H, Xu Y, et al. Hollow copper sulfide nanoparticles carrying ISRIB for the sensitized photothermal therapy of breast cancer and brain metastases through inhibiting stress granule formation and reprogramming tumor-associated macrophages. *Acta Pharm Sin B*. 2022;13(8):3471. doi:10.1016/j.apsb.2022.11.003
36. Kesharwani P, Ma R, Sang L, et al. Gold nanoparticles and gold nanorods in the landscape of cancer therapy. *Mol Cancer*. 2023;22(1):98. doi:10.1186/s12943-023-01798-8
37. Nejabat M, Samie A, Ramezani M, et al. An overview on gold nanorods as versatile nanoparticles in cancer therapy. *J Control Release*. 2023;354:221. doi:10.1016/j.jconrel.2023.01.009
38. Imran M, Ullah A, Saeed F, et al. Cucurmin, anticancer, & antitumor perspectives: a comprehensive review. *Crit Rev Food Sci Nutr*. 2017;58(8):1271. doi:10.1080/10408398.2016.1252711
39. Khan S, Imran M, Butt T, et al. Curcumin based nanomedicines as efficient nanoplatform for treatment of cancer: new developments in reversing cancer drug resistance, rapid internalization, and improved anticancer efficacy. *Trends Food Sci Technol*. 2018;80(8):8–22. doi:10.1016/j.tifs.2018.07.026
40. Rauf A, Imran M, Orhan IE, et al. Health perspectives of a bioactive compound curcumin: a review. *Trends Food Sci Technol*. 2018;74:45. doi:10.1016/j.tifs.2018.01.016
41. Aggarwal V, Tuli HS, Tania M, et al. Molecular mechanisms of action of epigallocatechin gallate in cancer: recent trends and advancement. *Semin Cancer Biol*. 2022;80:256. doi:10.1016/j.semcancer.2020.05.011
42. Li F, Qasim S, Li D, et al. Updated review on green tea polyphenol epigallocatechin-3-gallate as a cancer epigenetic regulator. *Semin Cancer Biol*. 2022;83:352. doi:10.1016/j.semcancer.2020.11.018
43. Jabłońska W, Wardęszkiewicz M, Kasprzak A, et al. Resveratrol - its properties, occurrence and health benefits. *J Educ Health Sport*. 2024;51:116. doi:10.12775/jehs.2024.51.009
44. Tang S, Deng X, Zhou J, et al. Pharmacological basis and new insights of quercetin action in respect to its anti-cancer effects. *Biomed Pharmacother*. 2020;121:109604. doi:10.1016/j.biopha.2019.109604
45. Harris Z, Donovan MG, Branco GM, et al. Quercetin as an emerging anti-melanoma agent: a four-focus area therapeutic development strategy. *Front Nutr*. 2016;3:00048. doi:10.3389/fnut.2016.00048
46. Chu M, Zheng C, Chen C, et al. Targeting cancer stem cells by nutraceuticals for cancer therapy. *Semin Cancer Biol*. 2022;85:245. doi:10.1016/j.semcancer.2021.07.008
47. Paulpandi M, Murugan K. Silymarin functionalized quantum cores as selective inhibitor of polo-like kinase 1, and preclinical antitumor activity in human breast cancer xenografts. *Ann Oncol*. 2019;30(6):ix6. doi:10.1093/annonc/mdz416.018
48. Khan H, Ullah H, Martorell M, et al. Flavonoids nanoparticles in cancer: treatment, prevention and clinical prospects. *Semin Cancer Biol*. 2021;69:200. doi:10.1016/j.semcancer.2019.07.023
49. Sferrazza G, Cortiet M, Brusotti G, et al. Nature-derived compounds modulating Wnt/β-catenin pathway: a preventive and therapeutic opportunity in neoplastic diseases. *Acta Pharm Sin B*. 2020;10(10):1814. doi:10.1016/j.apsb.2019.12.019
50. Shang L, Yang T, Yang C, et al. Metal ions-mediated self-assembly of nanomedicine for combinational therapy against triple-negative breast cancer. *Chem Eng J*. 2021;425:131420. doi:10.1016/j.cej.2021.131420
51. Gulla S, Reddy VC, Araveti PB, et al. Titanium dioxide nanotubes conjugated with quercetin function as an effective anticancer agent by inducing apoptosis in melanoma cells. *J Nanostruct Chem*. 2021;11(1):721–734. doi:10.1007/s40097-021-00396-8
52. Aiello P, Consalvi S, Poce G, et al. Dietary flavonoids: nano delivery and nanoparticles for cancer therapy. *Semin Cancer Biol*. 2021;69:150. doi:10.1016/j.semcancer.2019.08.029

53. Wei Y, Zhao X, Kariya Y, et al. Induction of apoptosis by quercetin: involvement of heat shock protein. *Cancer Res*. 1994;54(18):4952.
54. Ali M, Ali H, Rankin C, et al. Targeting heat shock protein 70 using gold nanorods enhances cancer cell apoptosis in low dose plasmonic photothermal therapy. *Biomaterials*. 2016;102:1–8. doi:10.1016/j.biomaterials.2016.06.017
55. Shin Y, Kim M, Lee ES, et al. RNA-Seq-guided triple-combination nano-system of gold nanocluster, quercetin, and docetaxel for ultimate synergistic photothermal-chemotherapy against MDR tumor. *Nano Today*. 2023;50:101862. doi:10.1016/j.nantod.2023.101862
56. Wang F, Wang B, Xu X, et al. Photothermal-responsive intelligent hybrid of hierarchical carbon nanocages encapsulated by metal−organic hydrogels for sensitized photothermal therapy. *Adv Healthcare Mater*. 2023;12(26):e2300834. doi:10.1002/adhm.202300834
57. Rafiq RA, Quadri A, Nazir LA, et al. A potent inhibitor of Phosphoinositide 3-Kinase (PI3K) and Mitogen Activated Protein (MAP) Kinase Signalling, Quercetin (3, 3', 4', 5, 7-Pentahydroxyflavone) promotes cell death in ultraviolet (UV)-B-Irradiated B16F10 melanoma cells. *PLoS One*. 2015;10(10):e0131253. doi:10.1371/journal.pone.0131253
58. Mishra SM. Flavonoids from ethanol extracts of euphorbia hirta inhibit melanoma growth and metastatic potential. *Ann Oncol*. 2019;30:117. doi:10.1093/annonc/mdz429.008
59. Cao H, Cheng C, Su T, et al. Quercetin inhibits HGF/c-Met signaling and HGF-stimulated melanoma cell migration and invasion. *Mol Cancer*. 2015;14(1):103. doi:10.1186/s12943-015-0367-4
60. Jana NR, Gearheart L, Murphy CJ. Seed-mediated growth approach for shape-controlled synthesis of spheroidal and rod-like gold nanoparticles using a surfactant template. *Adv Mater*. 2001;13(18):1389. doi:10.1002/1521-4095(200109)13:18<1389::AID-ADMA1389>3.0.CO;2-F
61. Zheng J, Cheng X, Zhang H, et al. Gold Nanorods: the Most Versatile Plasmonic Nanoparticles. *Chem Rev*. 2021;121(21):13342. doi:10.1021/acs.chemrev.1c00422
62. Liang J, Tian X, Zhou M, et al. Shikonin and chitosan-silver nanoparticles synergize against triple-negative breast cancer through RIPK3-triggered necroptotic immunogenic cell death. *Biomaterials*. 2024;309:122608. doi:10.1016/j.biomaterials.2024.122608
63. Zhu H, Huang C, Di J, et al. Doxorubicin-Fe(III)-Gossypol Infinite Coordination Polymer@PDA:CuO composite nanoparticles for cost-effective Programmed photothermal-chemodynamic-coordinated dual drug chemotherapy trimodal synergistic tumor therapy. *ACS Nano*. 2023;17(13):12544–12562. doi:10.1021/acsnano.3c02401
64. Xiang J, Liu K, Xu H, et al. Dual synergistic tumor-specific nanoparticles combating cancer self-defense for efficient chemo-immunotherapy. *Adv Sci*. 2023;10(29):2301216. doi:10.1002/advs.202301216
65. Xu D, Hu M, Wang Y, et al. Antioxidant activities of quercetin and its complexes for medicinal application. *Molecules*. 2019;24(6):1123. doi:10.3390/molecules24061123